Numerical investigation of the spatial integration effect on the velocity spectrum: Consequences in the wind or tidal turbine power spectrum

Philippe Druault, Jean-François Krawczynski

Journal Pre-proof

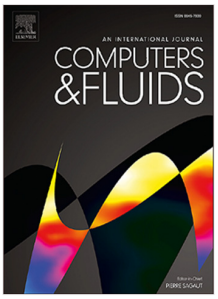

Numerical investigation of the spatial integration effect on the velocity spectrum: Consequences in the wind or tidal turbine power spectrum

Philippe Druault, Jean-François Krawczynski

PII: S0045-7930(22)00322-X
DOI: https://doi.org/10.1016/j.compfluid.2022.105729
Reference: CAF 105729

To appear in: *Computers and Fluids*

Received date : 24 February 2022
Revised date : 23 October 2022
Accepted date : 7 November 2022

Please cite this article as: P. Druault and J.-F. Krawczynski, Numerical investigation of the spatial integration effect on the velocity spectrum: Consequences in the wind or tidal turbine power spectrum. *Computers and Fluids* (2022), doi: https://doi.org/10.1016/j.compfluid.2022.105729.

Numerical investigation of the spatial integration effect on the velocity spectrum: consequences in the wind or tidal turbine power spectrum

Philippe Druault[a,*], Jean-François Krawczynski[a]

[a]*Sorbonne Université, CNRS, Institut Jean Le Rond d'Alembert, F-75005 Paris, France*

Abstract

We numerically investigate the effects of spatially integrating turbulent velocity signals and their impact on the power spectrum. Possible applications concern turbine power spectra. To this end, a 2D synthetic database built with the aim to mimic a realistic Atmospheric turbulent Boundary Layer (ABL) is used to infer previous observations from laboratory experiments. The size of the computational domain is supposed to be smaller than the integral length scale of the flow. In this case, it is demonstrated that, when spatially averaged along N direction(s), an anisotropic turbulent flow initially satisfying the Kolmogorov's "$-5/3$ law" exhibits a $-5/3 - 2N/3$ slope in the inertial range of its velocity spectrum. The synthetic database is further used to assess an equivalent turbine power spectrum computed from a 2D-spatial average (over the blade area) coupled with an average over the number of blades of the incoming velocity field. It is then confirmed that such an equivalent turbine power spectrum exhibits a power law decay exponent of $-11/3$ in the inertial range. Finally, several 1D databases are generated to study the spatial averaging procedure as a function of the number of points per integral length scale and the number of statistically independent velocity samples. We show that the additional $-2/3$ in the power law decay of the spatially averaged velocity spectrum is favorably observed in the case of a sufficient number of points (superior to 90) per integral length scale, regardless of the number of statistically independent velocity samples, even when the length of the domain is smaller than the integral length scale.

1. Introduction

The performances of wind or tidal turbines are usually estimated from the non-dimensional mean power coefficient C_p. Due to the tremendous amount

*Corresponding author
Email addresses: philippe.druault@sorbonne-universite.fr (Philippe Druault), jean-francois.krawczynski@sorbonne-universite.fr (Jean-François Krawczynski)

of numerical and experimental investigations, this parameter is now well predicted even if some questions still arise, e.g. about the reference velocity used to normalize the turbine power or about its dependence on the upstream flow conditions. However, the characterization of the unsteady turbine power variability remains a key issue for future improvements of this energy conversion device. In order to extend the lifetime and to increase the reliability of the wind and tidal turbine systems, a better understanding of the unsteady aerodynamic-hydrodynamic load on the blade is required. Furthermore, a better estimation of the turbine power variability would lead to a better control of the fluctuating electrical power feed into the grid, which is also a key problem.

It is now well admitted that the large-scale flow-structures embedded in the upstream turbulent flow have the largest contribution to the turbine power variability (Chamorro et al., 2015; Gaurier et al., 2020; Druault and Germain, 2022b). The flow scales related to the inertial range of the turbulent kinetic energy spectrum are also a source of power variability, but of smaller amplitude. However, their influence was poorly documented in previous works (Thé and Yu, 2017). The numerical simulations of unsteady Fluid Structure Interaction accounting for the physics processes between the unsteady small flow scales and the blade load remain hard and complex.

To characterize the small scales effect on the turbine performances, the inertial range of the turbine power-spectrum was analyzed. Recent experimental investigations emphasized that the spectra of the wind or tidal turbine outputs exhibited a power-law decay of $-11/3$ in their inertial frequency range (Tobin et al., 2015; Chamorro et al., 2015; Liu et al., 2017; Gaurier et al., 2020; Druault et al., 2022). While Tobin et al. (2015) associated this behavior to the rotational motion of the blade, Chamorro et al. (2015) suggested that this power-law arises from the functioning turbine which acts as a low-pass filtering of the upstream turbulent flow. Recently, Druault et al. (2022) interpreted this power-law decay as a spatial integration effect on the velocity field coupled with an average over the blades. They notably showed that the energy spectrum of high Reynolds number flows computed from velocity fields spatially averaged over N directions exhibited a power-law decay exponent of -5/3-2N/3. This last result was previously observed in some specific applications dealing with a spatial average over one direction. For instance, Bandi (2017) found that the power spectrum of a wind-turbines farm (with an average performed over the turbines number) follows a power law decay of $-7/3$ in the inertial range, whereas each wind-turbine was supposed to have a spectral power law of $-5/3$. Similarly, Katzenstein et al. (2010) observed the same behavior with a $-7/3$ power slope, by summing the turbine output spectrum over 20 individual wind turbines. Paraz and Bandi (2019) studied the effect of the spatially averaged velocity field on the resulting energy spectrum by considering Homogeneous and Isotropic Turbulence. The spatial average of the available velocity signals satisfying each a spectral power law decay of $-5/3$ in the inertial range, induced a modification of the power-law exponent towards $-7/3$. Sorensen and Schreck (2014) showed that the power spectral density of the thrust coefficient measured at one radial location of a single rotating blade exhibits a power law decay of $-7/3$ in the inertial range.

This also can be viewed as a resulting spatial average at this radial station. The recent contribution of Druault et al. (2022) proposed extensions to the previous works by investigating i) the spatial averaging (of the velocity field) effect on the kinetic energy spectrum for high Reynolds number flows with two non-homogeneous directions and ii) the effect of averaging over blades on the resulting turbine power-load spectrum. This study was based on Particle Image Velocimetry measurements therefore, on velocity fields sampled at 15 Hz on a coarse-grained grid. Further validations are thus required to fully characterize the spatial and/or blades averaging effect onto the turbine output spectrum. Consequently, this work subscribes to this requirement.

There are some differences that can not be ignored between wind turbine and tidal turbine fluid dynamics particularly because tidal flows are subjected to higher turbulence levels, a wavy environment, a free surface and a higher pressure blade loading than wind fields (Adcok et al., 2020). As a matter of fact, both wind and tidal turbines are driven by an unsteady high Reynolds number flow field satisfying Kolmogorov's $-5/3$ law in the inertial range of the velocity spectrum and exhibiting some vertical shear. In this sense, it is proposed to generate a synthetic velocity field representative of the incoming wind turbine flow. The analysis of the effect of its spatial averaging on the power-law decay in the inertial range of the velocity spectrum could then be generalized to incoming tidal turbine flow. It is based on a ad-hoc synthetic database designed to analyze the proposed spatial averaging effects. The interest of such a synthetic database is clear as it allows the investigation of multiple controllable parameters, e.g. the number of grid points, the sampling frequency and the time duration. Thus, a 2D synthetic database built with the aim to mimic a realistic Atmospheric turbulent Boundary Layer (ABL) is used to infer previous observations from laboratory experiments. In this case, it is assumed that the size of the computational domain is smaller than the integral length scale. However, the averaging effects discussed here are expected to depend on the number of points per integral length scale and the ratio of the length of the domain to the the integral flow length scale, that is the number of statistically independent velocity samples. Therefore, 1D databases are also generated to study these effects.

This paper is organized as follows. After the description of the mathematical procedure used to generate the velocity databases (§2), the 2D database is used in section 3 to study the spatial averaging effects on the velocity spectrum along one and two directions and its consequences on the turbine power spectrum. Finally, the effect of the integral length scale of the flow onto the spatially averaged velocity spectrum is investigated (§4).

2. Generation of synthetic instantaneous realizations of Atmospheric Boundary Layer flow

The purpose of this section is to describe the generation of a velocity database of a realistic turbulent Atmospheric Boundary Layer (ABL) flow field that could impact a wind turbine. Several spectral tensor models (as for instance (Kaimal

et al., 1972; Mann, 1994, 1998)) well suited to the ABL flow exist. They all satisfy the $-5/3$ law in the inertial frequency subrange and generally only differ in the low frequency range treatment due to distinct spatial coherence models, as confirmed by (Myrtvedt et al., 2020) in a recent analysis of the offshore wind turbine's response subjected to ABL flow generated with different models.
As previous studies stated that only the streamwise velocity component u (the x-direction is supposed to be the main flow direction) can be retained for the estimation of the turbine performance parameters (Bossuyt et al., 2017; Druault et al., 2022), we arbitrarily choose to restrict the data generation to this dominant component in a square cross-sectional extent ($L_y \times L_z$) which encompasses the entire rotor plane. The $y-$ and $z-$ directions correspond to the transverse and vertical directions respectively. Restricting the present work to only one velocity component is not an issue, as each velocity component has a similar power-law decay in the inertial range and the effect of the spatial averaging on the resulting velocity spectrum would be identical if the three velocity components were to be considered.
The Reynolds decomposition is assumed to be valid for the streamwise component of the velocity field, i.e.

$$u(y,z,t) = \overline{U}(y,z) + u'(y,z,t) \tag{1}$$

with $\overline{U}(y,z)$ the time-averaged component and $u'(y,z,t)$ its fluctuating counterpart.
For an ABL flow under neutral thermal conditions, the mean component $\overline{U}(z)$ is homogeneous along the transverse y-direction and it follows a logarithmic law along the vertical z-direction:

$$\overline{U}(y,z) = \frac{u^*}{\kappa} \ln\left(\frac{z}{z_0}\right) \tag{2}$$

where u^* is the friction velocity, z_0 is the roughness length and κ is the Von Karman constant for which a value of 0.4 is retained (Kaimal and Finnigan, 1994). Note that a mean velocity profile with a power law exponent can also be used without any effect on the following results.
The random fluctuating part (denoted realization in the following) will be determined from the specified statistical spectral properties of the ABL flow field.

2.1. Description of the wind model

The consolidated and widely used spectral Kaimal shear model (Kaimal et al., 1972) is used in this work. The velocity spectrum of the streamwise velocity component is expressed at a location (y,z) as:

$$S_u(y,z,f) = \frac{105 f_r}{(1+33f_r)^{5/3}} \frac{u^{*2}}{f} \tag{3}$$

with

$$f_r(y,z) = \frac{fz}{\overline{U}(y,z)}, \tag{4}$$

and $\overline{U}(y,z)$ is defined in equation 2. This model satisfies the Kolmogorov's "$-5/3$ law" in neutral atmospheric stratification. Such a model using a roughness length $z_0 = 0.03\,\mathrm{m}$ corresponds to a flow with a longitudinal integral scale of 110 m at 10 m above the surface at mid-latitudes (Simiu et al., 2019). To account for the flow coherence along the y- and z-directions, the Kaimal velocity spectrum is multiplied by a coherence function defined as follows Davenport (1961):

$$\gamma(f,r) = exp\left(-\left(a_y r_y + a_z r_z\right) f/U(y,z)\right) \tag{5}$$

where (a_y, a_z) are positive decay factors and (r_y, r_z) the distances between two points along the y- and z-directions.
As a first step, small values are retained for the coherence parameters, $(a_y, a_z) < (5dy, 5dz)$, with dy and dz the spatial mesh discretization sizes, to generate instantaneous velocity fields with larger integral length-scales than the computational domain sizes along the y- and z-directions. Although this is unrealistic in the vertical direction, it allows investigating the consequences of spatially averaged velocity signals in their power spectrum in the case of a flow with an integral length-scale larger than the spatial domain under consideration. The associated results are presented in section 3.
As a second step, to further study the effect of the number of points that describe the integral length scale of the flow on the spatially averaged velocity spectrum, one-dimensional velocity spectra are also considered along the homogeneous direction y. To do so, various values of the coherence parameter a_y associated with various turbulent integral length scales (see section 2.3.2) are considered.

2.2. Cholesky decomposition of the spectral Kaimal tensor and velocity field realizations

Once the spectral characteristics are specified for each point (y,z) of the grid, the next step is to determine each random velocity field realization at each point in the grid. Following previous works (Hekmati et al., 2013; Cheynet, 2018), for each frequency f, at any point in the grid (y,z), the Cholesky decomposition is applied to the velocity spectrum $S_u(y,z,f)$ (or $S_u(y,f)$ for one-dimensional flow field generation) to decompose it into a lower triangular matrix L and its conjugate transpose L^*:

$$S_u(y,z,f) = L(y,z,f)L^*(y,z,f) \tag{6}$$

Then, in the spectral domain, a realization of the random velocity field $\hat{u}$ is obtained:

$$\hat{u}(y,z,f) = \sum_{j=1}^{N_y \times N_z} L(y,z,f)e^{i\phi_j} \tag{7}$$

with $i^2 = -1$ and ϕ_j is an arbitrary random phase specified for each available grid point: $\phi_j = rand[0:1]\times 2\pi$. Finally, after determining $\hat{u}$ for all frequencies, an inverse Fourier transform is performed, and the real part corresponds to the random realizations of the flow field denoted $u'(y,z,t)$.

2.3. Parameters of the synthetic databases

2.3.1. Two-dimensional database

A domain size of $(L_y, L_z) = (100\,\mathrm{m}, 100\,\mathrm{m})$ is chosen, which corresponds to a total number of $N_y \times N_z = 150 \times 150 = 22500$ equally spaced points, with a spatial discretization $dy = dz = 0.67\,\mathrm{m}$. The mean flow field $\overline{U}(y, z)$ is generated according to equation 2 in the mesh grid related to the rotor area: $z \in [30\,\mathrm{m} : 130\,\mathrm{m}]$. This mean flow corresponds to the neutral atmospheric flow (figure 1, left-hand side). The values of $\overline{U}$ are $13.8\,\mathrm{m\,s^{-1}}$ and $16.7\,\mathrm{m\,s^{-1}}$ at the rotor tip (bottom and top respectively) and $15.8\,\mathrm{m\,s^{-1}}$ at the hub height. Knowing the mean velocity and spatial grid resolution, the temporal discretization dt is voluntarily fixed to 1/60 s (with a sampling frequency of $f_s = 60\,\mathrm{Hz}$). According to Shannon theory, the time step associated with the Nyquist frequency ($f_s/2$) is slightly inferior to $\frac{1}{2}\frac{dy}{max(\overline{U})}$ in agreement with the resolved spatial scales of the flow. As the sampling frequency f_s is known, the random generation of

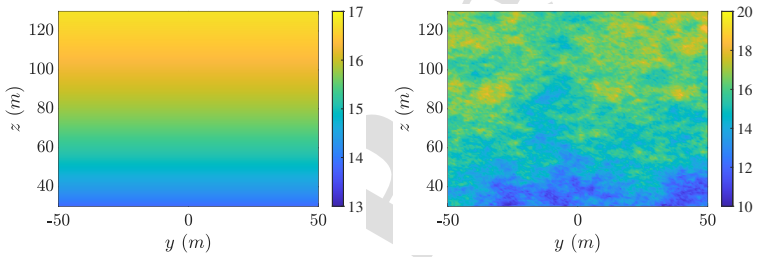

Figure 1: Left: mean streamwise velocity component. Right: example of a synthetic instantaneous velocity.

the fluctuating part of the velocity field (equation 7) is carried out for $N_t/2$ equally spaced frequencies from 0 to $f_s/2$. In the present work, N_t is fixed to 2^{16}, allowing a frequency resolution of $9 \times 10^{-4}\,\mathrm{Hz}$. Therefore, the synthetic database made of N_t instantaneous streamwise velocity fields is available on a regular meshgrid of $N_y \times N_z$ points. The total time duration $N_t \times dt$ is slightly superior to 18 min. The entire set of the database generation parameters is summarized in table 1. The size of the data fields $[N_y \times N_z, N_t]$ is retained

$N_y \times N_z$	$L_y \times L_z$	$dy = dz$	f_s	dt	N_t	Time duration
150×150	$100 \times 100\,\mathrm{m^2}$	$0.67\,\mathrm{m}$	$60\,\mathrm{Hz}$	$0.017\,\mathrm{s}$	2^{16}	$>18\,\mathrm{min}$

Table 1: Parameters of the 2D synthetic database.

to meet our computational capabilities, which are mainly sought out by the Cholesky decomposition.
An illustration of an instantaneous flow realization is shown in figure 1 (right-hand side).

N_y	L_y	dy	f_s	dt	N_t	Time duration
2001	100 m	0.05 m	60 Hz	0.017 s	2^{16}	>18 min

L_u (m)	1.0	2.7	5.3	7.0	13.2	29.8
$N_y L_u / L_y$	20	54	106	140	264	596

Table 2: Parameters of the 1D synthetic database used for generating 6 databases associated with the 6 different values of integral length scales L_u. $N_y L_u / L_y$ corresponds to the number of points describing the associated integral length scales.

2.3.2. One-dimensional databases

The objectives behind the generation of one-dimensional databases are twofold: a) to study the spatially averaged velocity spectrum as a function of the number of points per integral length scale and ; b) to study the spatially averaged velocity spectrum as a function of the ratio of the domain length to the turbulent integral length scale. Therefore, a fine spatial discretization is required, which, due to the high computational and memory costs, makes it impossible for us to use velocity databases with a larger dimension than one. $N_t = 2^{16}$ instantaneous velocity realizations are generated along the homogeneous direction y that extends to 100 m, at a specified height z_1 where the mean streamwise velocity is equal to 15 m s^{-1}. The spatial discretization is fixed to 0.05 m that corresponds to $N_y = 2001$ points (see table 2). On the basis of the procedure detailed above, 6 velocity databases related to different decay factors of the coherence function are generated. In each case, the integral length scale denoted L_u is determined from the two-point spatial correlation tensor, $R_{uu}(r_y)$ The integral scale,

$$L_u = \int_0^\infty R_{uu}(r_y) dr_y \tag{8}$$

measures the correlation length of the velocity fluctuations. The integral cannot practically extend to infinity, and the asymptotic behavior of the correlation tensor must be modeled for large separations r. A classical exponential model is used. Figure 2 shows the correlation functions for the 6 databases with the space variable for each correlation function normalized by its respective integral scale. The data collapse suggests that the length scale we measure is the characteristic scale of each correlation function. Therefore, the integral scale L_u is found to range from 1 m to 29.8 m which corresponds to variation of L_y/L_u from 100 to 3.3 (see table 2).

3. Velocity spatial integration effect on its power spectrum: consequences in the turbine power spectrum

In this section, we analyze the consequences of the 1D and 2D spatial integration of the velocity signal in its power spectrum. The consequences in the turbine power spectrum are then investigated.

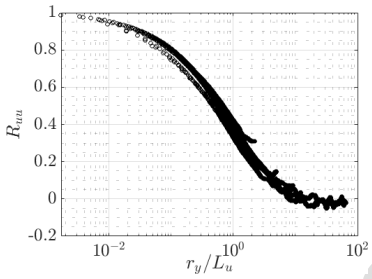

Figure 2: Velocity correlation functions as a function of the space variable r_y normalized by the integral scales for the corresponding correlation functions.

3.1. 1D spatial averaging effect on the velocity spectrum

The instantaneous velocity fields are used to investigate the effect of 1D spatial averaging on the velocity spectrum. Spatial averaging is successively performed over the homogeneous y-direction and over the non-homogeneous z-direction. The instantaneous velocity fields are extracted separately at positions y' and z', allowing us to perform the following 1D spatial average:

$$\mathcal{U}_y(z',t) = \frac{1}{N_y}\sum_{i_y=1}^{N_y} u(i_y,z',t) \tag{9}$$

$$\mathcal{U}_z(y',t) = \frac{1}{N_z}\sum_{i_z=1}^{N_z} u(y',i_z,t) \tag{10}$$

where $\mathcal{U}_y$ and $\mathcal{U}_z$ correspond to the spatially averaged realizations in the y- and z- directions, respectively. Note that the specific coordinates y' and z' have no incidence on the spectral results presented below. Unless explicitly mentioned, the Discrete Fourier Transform (DFT) computation is performed on the entire velocity signal of $N_t = 2^{16}$ points. This allows us to increase the frequency resolution and therefore to improve the spatial averaging efficiency, as demonstrated in section 3.2.

Figure 3 presents the frequency spectra $S_{\mathcal{U}_y}(f)$ and $S_{\mathcal{U}_z}(f)$ computed from the fluctuating parts $\mathcal{U}'_y(t)$ and $\mathcal{U}'_z(t)$, respectively, after subtracting their associated time averaged components, $\overline{\mathcal{U}_y}$ and $\overline{\mathcal{U}_z}$, respectively. The velocity spectrum of the original fluctuating component of the velocity field, $u'(y',z',t)$ satisfying the "$-5/3$ law" is also plotted for comparison. Regardless of the flow direction along which the average is computed, a spectral attenuation is observed in the inertial subrange. To check the asymptotic slope in the inertial range, the spectra are scaled by $f^{-5/3}$, $f^{-7/3}$ and f^{-3} and are represented in figure 3 (insert). The power-law exponent -3 comes from the relation $-5/3 - 2N/3$ mentioned in the introduction part with $N = 2$ in of case of an averaging performed over 2 dimensions. For the highest frequencies, the spectral values are

noticeably increased due to the aliasing effect, but both resulting spectra follow a power-law decay of $-7/3$ in the inertial sub-range. This result is in agreement with previous studies conducted in a homogeneous flow field (Paraz and Bandi, 2019; Bandi, 2017) and in homogeneous or non-homogeneous directions (Druault et al., 2022).

To state about the convergence towards the $-7/3$ decay power exponent with respect to the number of points used to compute the spatial average, some numerical tests are done by truncating the available velocity samples by taking equally spaced samples with various spatial discretizations. Regarding the homogeneous direction, the convergence is attained when the number of points used to compute the average approaches 100 which is in agreement with previous investigations (Paraz and Bandi, 2019; Druault et al., 2022). On the other hand, the convergence is faster for the non-homogeneous z-direction confirming previous observations (Druault et al., 2022). In the presence of a wind shear profile, as the time average velocity field $\overline{U}$ is included in $\mathcal{U}_z$, the degree of anisotropy at the small scales is increased faster than in the case of a uniform mean velocity profile. The local fluctuations at smaller scales are then expected to be smoothed out faster than in the presence of a uniform velocity profile.

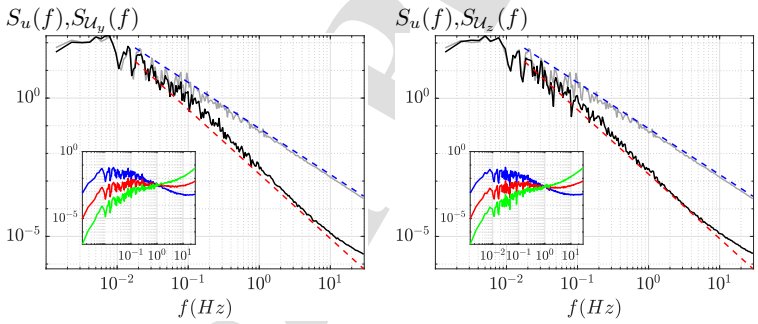

Figure 3: Superposition of the streamwise velocity spectrum $S_u(f)$ (gray continuous line) with the spectrum of the spatially averaged velocity field (black continuous line): along the y-direction (left), $S_{\mathcal{U}_y}$ and along the z-direction (right), $S_{\mathcal{U}_z}$, respectively. The dashed lines indicate a $-5/3$ (blue) and a $-7/3$ (red) scaling range. The insert shows $S_{\mathcal{U}_y}$ (left) and $S_{\mathcal{U}_z}$ (right) scaled by: $f^{-5/3}$ (blue), $f^{-7/3}$ (red) and f^{-3} (green).

3.2. Effect of the time duration and sampling frequency on the FFT applied to the spatially averaged velocity field

Besides the number of points used to calculate the spatial average, the DFT computation is also a function of both the time duration, i.e., frequency discretization, and the sampling frequency (related to the frequency domain $[0 : f_s/2]$ in the spectral analysis) of the available signal. The effect of these two parameters on $S_{\mathcal{U}_y}$ and $S_{\mathcal{U}_z}$ is investigated in the following.

First, the spatially averaged velocity field (equations 9-10) is successively determined for several time duration of instantaneous realizations: $N_t/16$, $N_t/8$, $N_t/4$, $N_t/2$ and N_t, the last being considered as a reference. Figure 4 (left-hand side) shows the scaled spectra $S_{\mathcal{U}_y}(f)/f^{-7/3}$ and $S_{\mathcal{U}_z}(f)/f^{-7/3}$, computed from both spatial averages of the velocity field along the y- and z-directions. It is observed for both cases that: i) the aliasing effect in the high-frequency domain (due to the DFT application) is more pronounced when the number of realizations decreases, ii) the presence of noise (also due to the DFT application) is accentuated when a small number of flow realizations is considered, iii) the smoothing effect due to spatial averaging is less efficient when the number of realizations is small.
Second, the spatial average computation (equations 9-10) is applied to velocity fields sampled at different frequencies: $f_s/5$, $f_s/4$, $f_s/3$, $f_s/2$ and f_s, the last one considered as the reference. Figure 4 (right-hand side) shows the scaled spectra $S_{\mathcal{U}_y}(f)/f^{-7/3}$ and $S_{\mathcal{U}_z}(f)/f^{-7/3}$, computed from both spatial averages (along the y- and z-directions). Overall, whatever is the sampling frequency, a plateau is observed, which confirms the decay exponent of $-7/3$. Note that the plateau is larger for the largest value of the sampling frequency as the smoothing process applied to small scales is expected to be more efficient. This also emphasizes that when the time duration is sufficiently long, the sampling frequency has a smaller effect on the spatially averaged velocity spectrum. This is similar to the treatment of non-homogeneous direction for which the convergence towards $-7/3$ is accelerated by the mean shear profile.

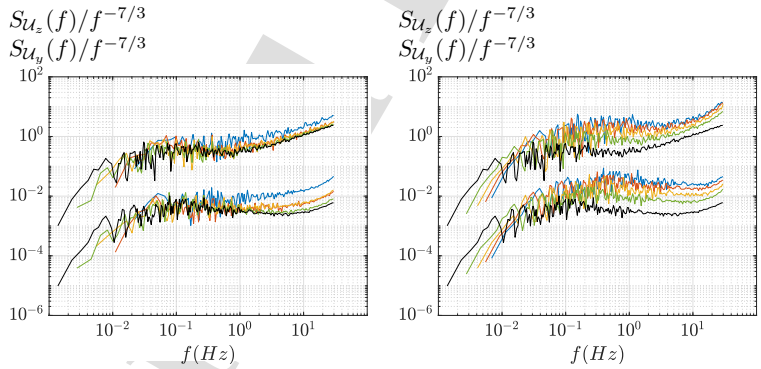

Figure 4: Streamwise velocity spectrum of the spatially averaged velocity field along the y-direction, and along the z-direction (shifted upwards by a factor of 10^2 for better visibility). Left: as a function of N_t. black: N_t, green: $N_t/2$, orange: $N_t/4$, red: $N_t/8$, blue: $N_t/16$. Right: as a function of the sampling frequency, f_s. black: f_s, green: $f_s/2$, orange: $f_s/3$, red: $f_s/4$, blue: $f_s/5$. All scaled by $f^{-7/3}$.

3.3. 2D spatial averaging effect on the velocity spectrum

The spatial averaging is now performed simultaneously over both the homogeneous y- and non-homogeneous z-directions:

$$\mathcal{U}_{yz}(t) = \frac{1}{N_y N_z} \sum_{i_y=1}^{N_y} \sum_{i_z=1}^{N_z} u(i_y, i_z, t) \tag{11}$$

Figure 5 shows the velocity spectrum $S_{\mathcal{U}_{yz}}(f)$ calculated from the fluctuating part of $\mathcal{U}_{yz}(t)$. To better understand the behavior in their inertial subrange, their scaling with $f^{-5/3}$ or $f^{-7/3}$ or f^{-3} or $f^{-11/3}$ is again considered. Although the aliasing effect still alters the interpretation of these spectra in the high-frequency domain, a -3 power decay exponent is clearly visible in the inertial range. This is in agreement with previous work (Druault et al., 2022) in which it was shown that the spectra exhibited a power decay exponent of $-5/3-2\times2/3 = -3$, where the coefficient 2 stands for the number of dimensions in which spatial averaging of the velocity field is performed.

In order to check for the convergence of the power law exponent α, the spectrum of the following velocity field

$$\mathcal{U}_{N_p}(t) = \frac{1}{N_p} \sum_{i_y=1}^{N'_y} \sum_{i_z=1}^{N'_z} u(i_y, i_z, t) \tag{12}$$

is determined for various $N_p = N'_y \times N'_z$ with $N'_y = N'_z$. A linear regression is performed in the inertial range, which is suppose to be contained in the following frequency domain $[0.3 : 2]$ Hz, kept constant in each case. The evolution of α as a function of N_p emphasizes its fast convergence towards -3 (see figure 5, right-hand side). A small oscillation around $\alpha = 3$ is observed. This is due to the DFT computation and the frequency interval retained to compute the linear regression. Consequently, performing a 2D spatial average over two non-homogeneous directions can be viewed as two consecutive spatial averages in each direction. Therefore, a similar additional attenuation (of $-2/3$) is observed in the inertial subrange.

3.4. The turbine power spectrum: towards an interpretation of its power decay exponent

As stated in the introduction, the turbulent flows related to the tidal stream and the wind field show some similarities, especially in the inertial range of the associated velocity spectra where a similar power decay exponent of $-11/3$ was observed (Tobin et al., 2015; Chamorro et al., 2015; Liu et al., 2017; Gaurier et al., 2020; Druault et al., 2022).

Usually, the knowledge of the mean velocity profile $\overline{U}$ enables the turbine power estimation by integrating the $\overline{U}^3$ profile over the rotor-disk area (Bossuyt et al., 2017; Bandi, 2017; Druault et al., 2022). Similarly, the turbine thrust is calculated from the integration of the squared of the velocity profile over the rotor-disk area. In the following, only the turbine thrust is considered and similar

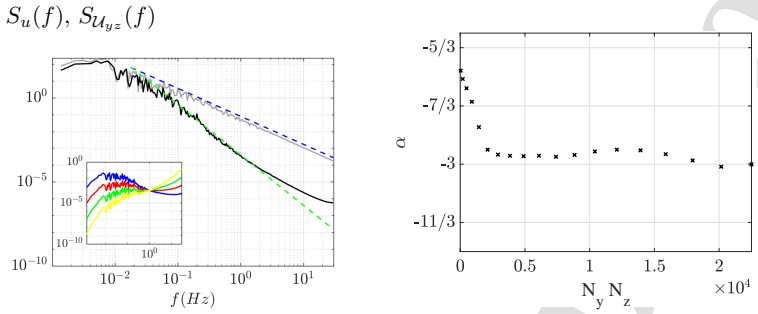

Figure 5: Left. Superimposition of the streamwise velocity spectrum $S_u(f)$ (gray continuous line) with the spectrum of the spatially averaged velocity field along both the y-direction and the z-direction (black), $S_{\mathcal{U}_{yz}}(f)$. The dashed lines indicate a $-5/3$ (blue) and a -3 (green) scaling range. The insert shows $S_{\mathcal{U}_{yz}}(f)$ scaled by: $f^{-5/3}$ (blue), $f^{-7/3}$ (red), f^{-3} (green) and $f^{-11/3}$ (yellow). Right. Power spectral law exponent as a function of $N_p = N_y \times N_z$ with $N_y = N_z$.

expressions can be derived for the turbine power. Therefore, as a first approximation (Bossuyt et al., 2017; Bandi, 2017; Druault et al., 2022), the fluctuating part of the turbine thrust is linearly dependent on the fluctuating part of the spatially averaged velocity field over the rotor area:

$$T'(t) \simeq K_1 \mathcal{V}'(t) \tag{13}$$

where K_1 is a constant depending on the thrust coefficient, the rotor area, the fluid density, and the time average velocity (Druault et al., 2022). In equation 13, $\mathcal{V}'$ represents the fluctuating part of the streamwise velocity component, spatially averaged over the rotor area. This equation is generally used when considering the numerical approach of the disk average. To assess the instantaneous fluctuating power resulting from the N_b blades, we propose to only retain the velocity field which is instantaneously seen by the wind turbine along the blade (Sorensen et al., 2002; Druault et al., 2022):

$$T'(t) \simeq K_2 \sum_{i=1}^{N_b} \mathcal{V}'_i(t) \tag{14}$$

where K_2 is a constant depending on the thrust coefficient, the blade area, the fluid density, and the time average mean velocity (Druault et al., 2022). $\mathcal{V}'_i$ is the fluctuating part of the spatially averaged velocity field on the i^{th} blade area. The spectral computation of the power is then assessed as follows:

$$S_{T'}(f) \simeq K_2 \widehat{\sum_{i=1}^{N_b} \mathcal{V}'_i}(f) \tag{15}$$

Note that the generated synthetic ABL velocity field database does not exactly correspond to the velocity field $\mathcal{V}$ that is expected to impact the blades.

In fact, flow induction due to turbine blockage, together with the blade rotational motion causing an additional circumferential velocity could have been taken into account. Druault and Germain (2022a) have recently observed that the turbine blockage effect (also called turbine induction) induces modifications of the mean shear profile in front of the turbine by altering the incoming mean shear velocity profile. The power law decay ($-5/3$) of the velocity spectra in front of the turbine was also shown to be similar to that in the absence of the turbine (Druault et al., 2022; Druault and Germain, 2022a), meaning that the additional circumferential velocity component does not have an impact on the shape of the velocity spectrum in the inertial range.
We can even assume that, as the induction of the turbine accentuates the mean shear of the incoming flow, an increase in the convergence of the spectrum computed from the spatially averaged velocity field could be expected.
Therefore, the synthetic velocity database designed for this work can be used as a first approximation to assess the previous analysis (Druault et al., 2022) concerning the coupled effect of the spatial and blade averaging in the inertial range of the velocity spectrum.

3.4.1. Application

To approach a realistic wind turbine configuration, a rotor diameter of $D = L_y = L_z = 100\,\mathrm{m}$ is specified with its hub located at 80 m above sea level. The blade is of a rectangular area with a length of $R = 45\,\mathrm{m}$ and a width of $l = 6\,\mathrm{m}$. The instantaneous field viewed by the i^{th} blade is then expressed as follows:

$$\mathcal{U}_i(t) = \frac{1}{N_{pb}} \sum_{\theta=1}^{N_{\theta b}} \sum_{r=1}^{N_{rb}} u(r(t), \theta(t), i) \tag{16}$$

where $N_{pb} = N_{\theta b} \times N_{rb}$ is the total number of points on the grid that sweep the blade area. At $t = 0$, each blade is related to a specific area that corresponds to N_{pb} points (see figure 6, left column). Then, to reproduce the rotation of the blade, each blade area is rotated in the plane. Consequently, the angular position $\theta(t)$ and the radial position $r(t)$ related to each blade change at each time step as a function of the Tip Speed Ratio (TSR). The TSR is equal to $\omega R / \langle U \rangle$, with ω the rotational speed of the rotor, and $\langle U \rangle = 15.4\,\mathrm{m\,s^{-1}}$ the ensemble average of the velocity database. An illustration of some instantaneous velocity fields retained to reproduce the field impacting a three- and a six-blades horizontal turbine is depicted in figure 6. In this figure, the turbine is supposed to have a TSR of 7 and the three instantaneous velocity fields correspond to three instants with 200 time steps ($dt = 1/f_s$) between each. In the following, four TSR are considered. The corresponding blade frequency passage f_b and rotor velocities (denoted RPM) are indicated in table 3. As the total number of realizations $N_t = 2^{16}$ is fixed, each TSR configuration leads to different numbers of cycles N_{tr} that are also referenced in this table. Furthermore, two turbines equipped with three and six blades are successively considered. The associated blade frequency passages $3f_b$ and $6f_b$ are given in table 3.

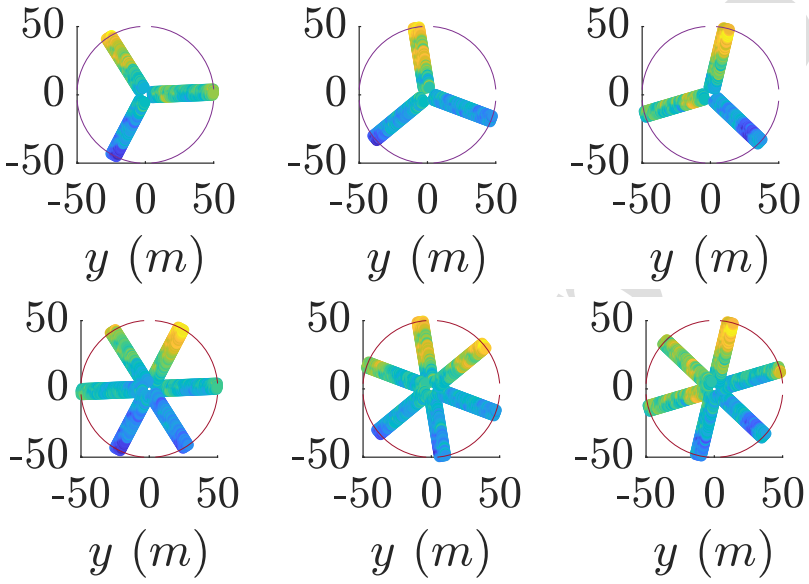

Figure 6: Three instantaneous velocity fields viewed by the three blades (200 time steps between each). These representations are associated with a TSR of 7.

TSR	f_b (Hz)	$3f_b$ (Hz)	RPM (tr/min)	N_{tr}
2	0.111	0.333	86.40	1575
3	0.166	0.497	58.00	1048
7	0.387	1.161	24.68	449
10	0.553	1.658	17.28	315
14	0.774	2.321	12.34	224

Table 3: Parameters of the turbine characteristics using various TSR and equipped with three and six blades.

For N_b blades, an approximation of the thrust PSD is obtained by computing

$$S_{T'}(f) \simeq \widehat{\sum_{i=1}^{N_b} \mathcal{U}_i'}(f) \tag{17}$$

This equivalent spectral approximation is then related to a 2D spatial average over the blade area coupled with an average over the blade number.

3.4.2. Spectral computation of the equivalent turbine thrust applied at a fixed radius

A first analysis is performed considering only the turbine thrust applied at a radial distance r from the hub. The following velocity field is used to

approximate the turbine thrust at radius r_0:

$$\mathcal{U}_i(r_0,t) = \frac{1}{N_{\theta b}} \sum_{\theta=1}^{N_{\theta b}} u(r_0, \theta(t), i) \tag{18}$$

and an approximation of the thrust PSD is obtained by computing the following associated velocity PSD:

$$S_{T^1_{r_0}}(f) = \widehat{\mathcal{U}_1(r_0,t)}(f) \text{ and } S_{T^{N_b}_{r_0}}(f) = \widehat{\sum_{i=1}^{N_b} \mathcal{U}_i(r_0,t)}(f) \tag{19}$$

with $S_{T^1_{r_0}}$ and $S_{T^{N_b}_{r_0}}$ the spectra computed from one blade and averaged over N_b blades, respectively. In the following, r_0 is set to 40. These spectra are calculated from four TSR (3, 7, 10 and 14) mentioned in table 3. Figures 7 and 8 present the scaled spectra for each TSR configuration. To appreciate the power-law decay in the inertial frequency range, the thrust spectra scaled by $f^{-5/3}$, $f^{-7/3}$, f^{-3} or $f^{-11/3}$ are superimposed on each graph. Note that in figure 8, N_b is equal to 3.

Whatever the TSR values are, each PSD exhibits the associated blade passage frequency, f_b and its harmonics (figure 7) and $3f_b$ and its harmonics (figure 8). Even if these frequency peaks quite modify the inertial range of the velocity spectra, we observe that when dealing with the one-blade configuration ($S_{T^1_{r_0}}$, figure 7) the thrust PSD mainly exhibits a power decay exponent of $-7/3$ which corresponds to the power law decay observed in section §3.1. This result, which is directly related to the 1D spatial averaging over the radius of the blade, is in agreement with previous numerical investigations of the thrust PSD obtained at a fixed radial position (Sorensen and Schreck, 2014).
Conversely, when regarding the three-blades configuration ($S_{T^3_{r_0}}$, figure 8), a power-law decay of -3 is quite noticeable for each spectrum regardless of the TSR value. This emphasizes that these PSD result from a double averaging over the blade radius and over the blades. This is then consistent with the 2D spatial averaging effect observed in section §3.3. Even if the number N_b is very small, the convergence of the power-law decay is accelerated with the rotational motion of the blade.

Therefore, these preliminary results show that the average over the number of blades can be viewed as a spatial average, and a similar effect is observed in the inertial range of the resulted thrust PSD.

3.4.3. Spectral computation of the equivalent turbine thrust

The three-blades and six-blades configurations are then successively considered to investigate the equivalent turbine thrust spectrum computed from the following velocity field:

$$\sum_{i=1}^{N_b} \mathcal{U}_i(t) = \sum_{i=1}^{N_b} \left[\frac{1}{N_{pb}} \sum_{\theta=1}^{N_{\theta b}} \sum_{r=1}^{N_{rb}} u(r(t), \theta(t), i) \right] \tag{20}$$

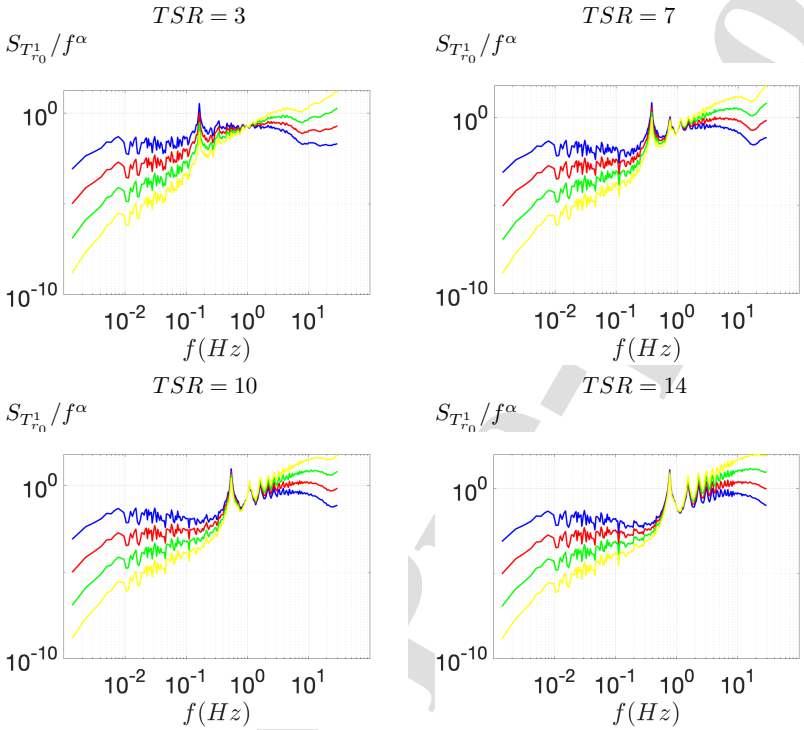

Figure 7: Equivalent turbine thrust spectra $S_{T^1_{r_0}}$ scaled by: $f^{-5/3}$ (blue), $f^{-7/3}$ (red), f^{-3} (green), $f^{-11/3}$ (yellow). The turbine thrust is estimated at a fixed radius for only one blade at four TSR values.

where $N_{pb} = N_{\theta b} \times N_{rb}$ is equal to 544 for the present blade area ($R = 45$m, $l = 6$) corresponding to $(N_{\theta b}, N_{rb}) = (8, 68)$.

Figure 9 represents the equivalent scaled turbine thrust spectrum, denoted $S_{T_{eq}}$, with $N_b = 3$ for selected TSR values. Similar representations (not shown here) are obtained for $N_b = 6$.

Note that in the present test case, only the smaller TSRs are retained in order to avoid any misunderstanding in the high-frequency domain which is polluted by the blade frequency passage (see table 3). Blade passage frequencies $3f_b$ ($N_b = 3$) are clearly identified and are in agreement with the values indicated in table 3. They depend both on the blade number and on the TSR values. Even if these frequency peaks pollute the inertial frequency range of the spectra, a distinguishable power-law decay of $-11/3$ is apparent in each spectrum. Consequently, previous results (Druault et al., 2022) for a turbulent flow with a larger integral length scale than the rotor diameter are confirmed,

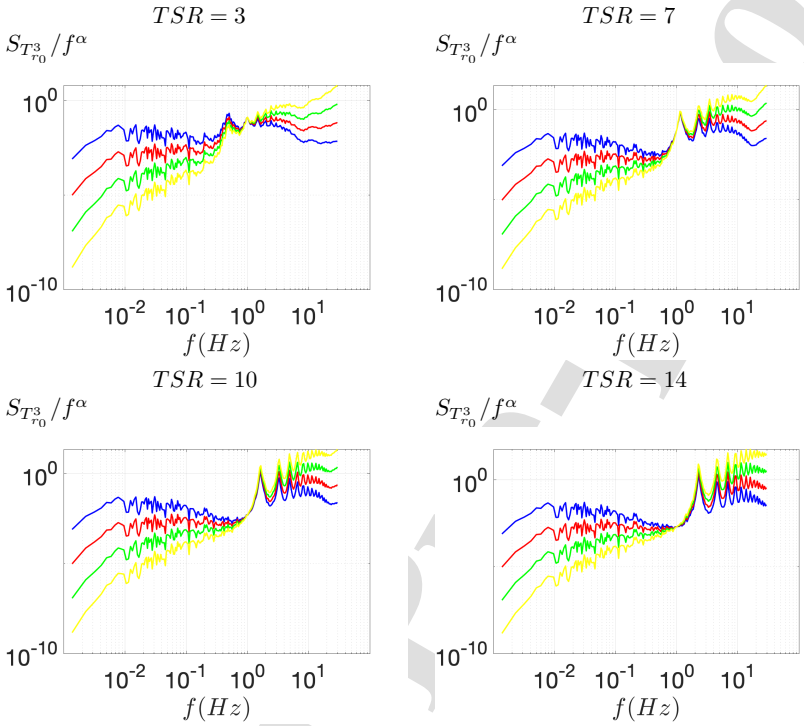

Figure 8: Equivalent turbine thrust spectra $S_{T^3_{r_0}}$ scaled by: $f^{-5/3}$ (blue), $f^{-7/3}$ (red), f^{-3} (green), $f^{-11/3}$ (yellow). The turbine thrust is estimated at a fixed radius for three rotating blades at four TSR values.

that is, the spectrum of the 2D spatially averaged velocity field coupled with an integration over the blade exhibits a power-law decay exponent of $-11/3$ in its inertial range. However, as stated in the introduction part, the spatial averaging procedure and its consequence on the resulted spectrum mainly depends on the the statistically independence and/or the number per integral length scale. This is the subject of the next section.

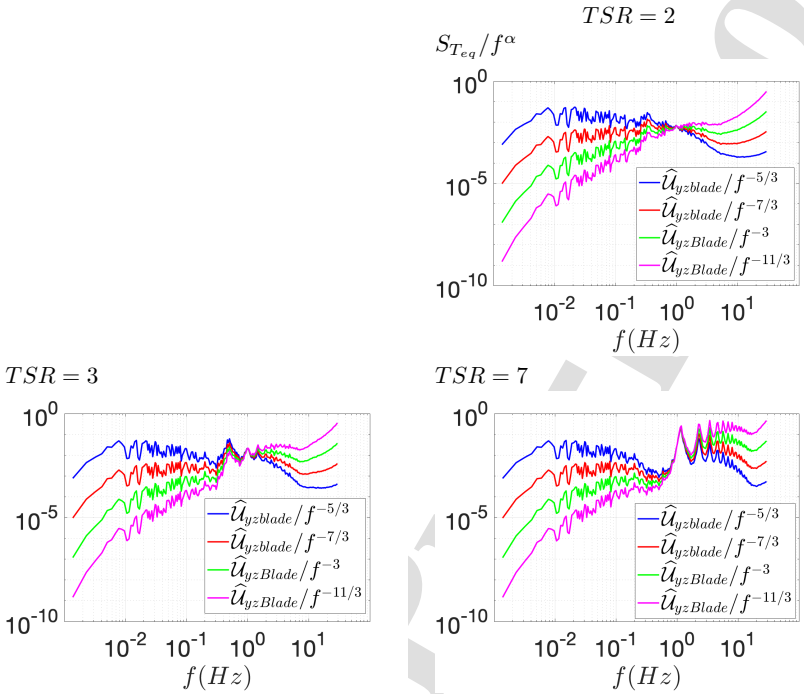

Figure 9: Equivalent scaled turbine thrust spectra computed from the 2D spatial average over blade area coupled with the blade average over the $N_b = 3$ blades of the instantaneous velocity field. Each graph corresponds to a different TSR value and the thrust spectra $S_{T_{eq}}$, are scaled by : $f^{-5/3}$ (blue), $f^{-7/3}$ (red), f^{-3} (green), $f^{-11/3}$ (yellow).

4. Effect of the flow integral length scale on the spatially averaged velocity spectrum

For each realization of the 1D database generated as described in section 2.3.2, the velocity field is spatially averaged as follows:

$$\mathcal{U}_{N_y}(t) = \frac{1}{N_y} \sum_{i_y=1}^{N_y} u(i_y, t) \tag{21}$$

and the spectrum is computed from this averaged velocity field. As the number of points along the y-direction ($N_y = 2001$, $L_y = 100\,\mathrm{m}$, $dy = 0.05\,\mathrm{m}$) is kept fixed for all databases, a different number of points is used to describe the integral length scale $N_y L_u / L_y$ (see table 1). Figure 10 shows the superposition of the spatially averaged velocity spectra $S_{\mathcal{U}_{N_y}}(f)$ scaled with $f^{-5/3}$ and $f^{-7/3}$, respectively.

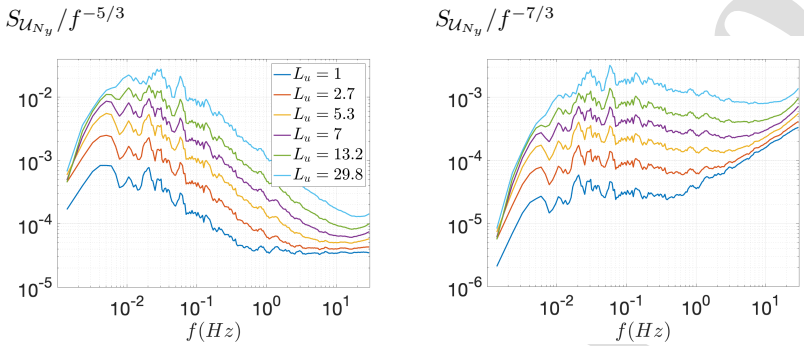

Figure 10: Superimposition of compensated (left $f^{-5/3}$, right $f^{-7/3}$) spatially averaged velocity spectra computed from the six database having varying integral flow scales indicated in the legend of the graph (see table 2).

As the integral length scale increases, the power-law decay exponent in the inertial range tends to $-7/3$ as illustrated by the quasi-plateau observed in the compensated spectra in figure 10, right. Conversely, for the case of the smallest integral length scale ($L_u = 1\,\mathrm{m}$), the power law decay of $-7/3$ is only observed over a restricted range in the mid-frequency domain, and the $-5/3$ power law decay is apparently recovered at high frequencies. Even if aliasing effects occur in this frequency domain, it may also be a consequence of the ratio of the domain length to the integral length scale (that is, the number of statistically independent samples) or the number of points that actually describe the integral length scale.

These databases are now successively truncated by limiting the length of the domain $L_p \leq L_y$ and/or by modifying the spatial discretization $dp \geq dy$ leading to considering $N_p \leq N_y$ equally spaced velocity samples:

$$\mathcal{U}_{N_p}(t) = \frac{1}{N_p} \sum_{i_p=1}^{N_p} u(i_p, t) \tag{22}$$

Therefore, the effect of the number of points that describe the integral length scale $N_p L_u/L_p = L_u/dp$ and the effect of the number of statistically independent samples $N_i = L_p/L_u$ can be investigated based on the analysis of the associated spectra $S_{\mathcal{U}_{N_p}}$.

First, three cases are considered for which $L_p = aL_u$ with $a = 1,\ 0.8$ and 0.5. This means that all samples are statistically dependent and then it can be related to the previous application presented in the section 3. The case $L_u = 29.8\,\mathrm{m}$ is retained as it presents the largest possible number of points that describe the integral scale $N_y L_u/L_y = 596$ (see table 2). N_p equally spaced points are extracted among the available ones, which then leads to the consideration of varying spatial discretization $dp = L_p/N_p$. Figure 11 shows the spatially

averaged velocity spectra compensated for $f^{-5/3}$ and $f^{-7/3}$ as a function of $N_p L_u/L_p = L_u/dp$. The higher the number of points per integral length scale, the more likely the spectral power-law decay converges toward $-7/3$ in the inertial range.

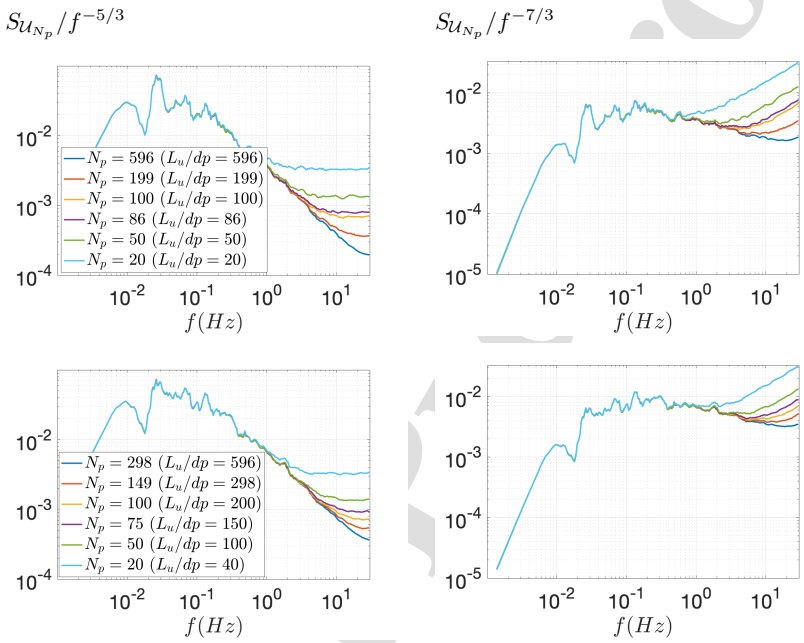

Figure 11: Superimposition of compensated (left $f^{-5/3}$, right $f^{-7/3}$) spatially averaged velocity spectra computed from various velocity samples allowing the investigation of N_p ($N_p L_u/L_p$) numbers (indicated in the graph) for two values of the length of the domain, Top: $L_d = L_u$. Bottom: $L_d = 0.5L_u$, with $L_u = 29.8$m.

It is interesting to observe that even if the domain length is half the integral length scale, quite similar results are obtained to those of $L_p = L_u$, when it comes to the equivalent number of points per integral length scale. As the aliasing effect occurs at the highest frequencies, it is observed that when $N_p > 90 - 100$, the inertial range of the spatially averaged velocity exhibits a power-law decay of $-7/3$ for $L_p \approx L_u$ (and even for $L_p = 0.5L_u$). This confirms previous experimental investigations (Paraz and Bandi, 2019; Druault et al., 2022) and results presented in section 3.1.

To go further, figure 12 presents the same compensated spectra but now computed from the spatially averaged of exactly $N_p = 100$ equally spaced velocity realizations covering each length domain $L_p = aL_u$ with $a = 1,\ 0.8$ and 0.5. As L_p varies, $N_p L_u/L_p = L_u/dp$ changes in each case (see table 2).

Globally similar results are observed regardless of the value of the domain

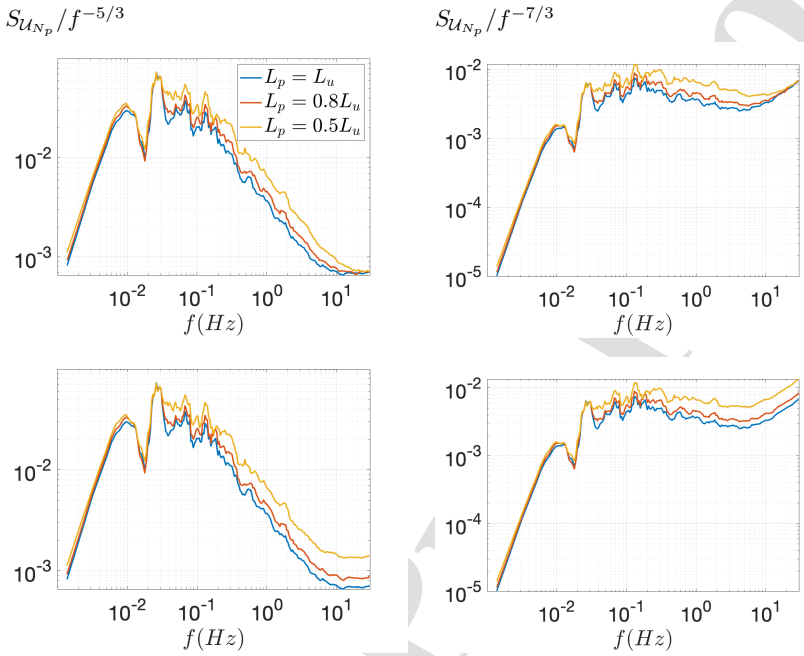

Figure 12: Superimposition of compensated (left $f^{-5/3}$, right $f^{-7/3}$) spectra computed:
top-line: from the spatially average of exactly $N_p = 100$ equally spaced velocity realizations with varying dp
bottom-line: from the spatially average of various N_p velocity realizations having the same equivalent number of point per integral length scale $N_pL_u/L_p = 100$
all covering the three values of the length domain $L_p = L_u,\ 0.8L_u,\ 0.5L_u$. $L_u = 29.8$m.

length and then independently of the spatial discretization. Figure 12 also presents the compensated spectra calculated from the spatially averaged of various N_p velocity realizations covering each length domain $L_p = L_u,\ 0.8L_u,\ 0.5L_u$ and having the same spatial discretization $dp = 0.3$ m that is, the same equivalent number of points per integral length scale $N_pL_u/L_p = L_u/dp = 100$. In this case, the number N_p varies as a function of dp, but always remains superior to 50 (see table 4). Quasi-similar spectra are observed regardless of the N_p number. It then appears that whatever the spatial extent of the domain related to the integral length scale, with $L_p \in [0.5 : 1] \times L_u$, when a sufficient number of points per integral length scale is retained, the spatially average velocity spectrum exhibits a power-law decay of $-7/3$ in the inertial range.

As a second analysis, the effect of the number of statistically independent samples, N_i, on the resulting spatially averaged velocity spectra is considered. We consider three cases for which $N_pL_u/L_p = 100,\ 50,\ 20$ for the associated inte-

L_p (N_i)	N_p (L_u/dp)	N_p (L_u/dp)	N_p (L_u/dp)	N_p (L_u/dp)	N_p (L_u/dp)	N_p (L_u/d_p)
L_u (1)	596(596)	199 (199)	100 (100)	86 (86)	50 (50)	20 (20)
$0.8L_u$ (0.8)	477 (596)	239 (298)	96 (120)	80 (100)	53 (66)	20 (25)
$0.5L_u$ (0.5)	298 (596)	149 (198)	100 (200)	75 (150)	50 (100)	20 (40)

Table 4: Parameters of the velocity databases used to compute its average spectrum (see figure 11). Each database is related to a specific length domain L_p expressed as a function of L_u the integral length scale (or $N_i = L_p/L_u$), with $L_u = 29.8$m. The number of equally spaced realizations, N_p and the (equivalent) number of points per integral length scale, $N_pL_u/L_p = L_u/dp$, are also provided.

N_pL_u/L_p (L_u)	N_i (N_p)	N_i (N_p)	N_i (N_p)	N_i (N_p)	N_i (N_p)	N_i (N_p)
106 (5.3m)	1 (106)	3 (318)	5 (530)	10 (1060)	15 (1590)	18.9 (2001)
54 (2.7m)	1 (54)	5 (270)	10 (540)	20 (1080)	30 (1620)	37.6 (2001)
20 (1m)	1 (20)	20 (400)	40 (800)	60 (1200)	80 (1600)	100 (2001)

Table 5: Parameters of the velocity databases used to compute its average spectrum (see figure 13). Each database is related to a specific number of points per integral length scale $N_pL_u/L_p = 106,\ 54, 20$ associated with $L_u = 5.3,\ 2.7$ 1m respectively and to varying numbers of independent statistical velocity samples $N_i = L_y/L_u$ are considered.

gral length scale values: $L_u = 5.3,\ 2.7,\ 1$m and in each case the velocity spectra are computed from the average of velocity samples using various $N_i = L_y/L_u$ numbers (see table 5). Figure 13 shows the resulting spatially averaged velocity spectra compensated for $f^{-5/3}$ and $f^{-7/3}$, respectively. The compensated spectra exhibit two plateaus that correspond to two different power-law decay exponents: a $-5/3$ in the high-frequency domain (which may also be related to the aliasing effect) and a $-7/3$ in the mid-frequency domain. As N_pL_u/L_p increases, the $-7/3$ plateau is extended more to the high-frequency domain. However, the effect of the N_i number seems globally not dependent on the N_pL_u/L_p number. Whatever its value, some similar tendencies occur when N_i increases: the frequency domain for which the power-law decay exponent is $-5/3$, slightly extends to the mid-frequencies. The normalized one-point velocity spectrum (without any spatial average) is also represented in the bottom line of figure 13 to show the behavior of an initial reference velocity sample satisfying Kolmogorov power law decay (Equation 3). It is expected that increasing by a very high factor the number of statistically independent samples would allow us to recover the initial power-law decay of the one-point velocity spectrum. The additional $-2/3$ observed in the inertial range of $S_{\mathcal{U}_{N_p}}$ is preferentially observed for a reduced number of statistically independent velocity samples. The spatial filtering process that induces an additional $-2/3$ cannot be attributed to a statistical operation. The use of numerous statistically independent velocity samples limits the spatial average effect as the spatial average of numerous independent samples dominates the spatial average performed along the integral length scale itself, in this case.

Previous results demonstrate that the spectrum of the spatially averaged

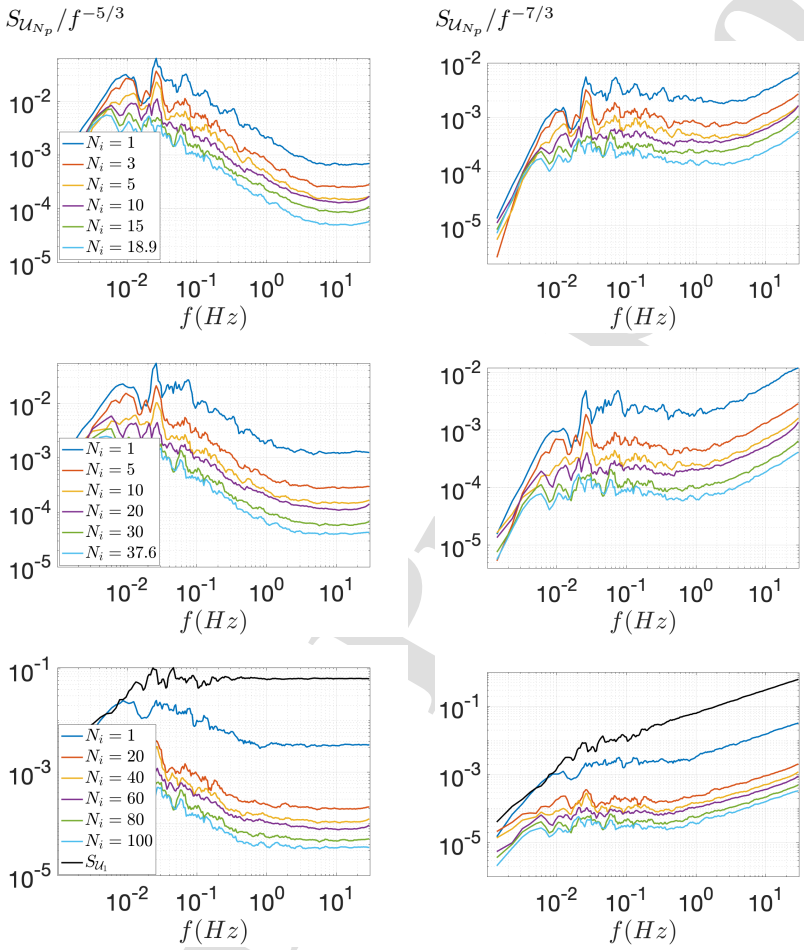

Figure 13: Superimposition of compensated (left $f^{-5/3}$, right $f^{-7/3}$) spectra computed from the spatially average of $N_p = 100$ equally spaced velocity samples covering $N_i = L_p/L_u$ integral length scales (this number is indicated in each graph). Top: $L_u = 5.3$m ($N_p L_u/L_p = 100$). Center: $L_u = 2.7$m ($N_p L_u/L_p = 50$). Bottom: $L_u = 1$m ($N_p L_u/L_p = 20$). In bottom graphs, the normalized one-point velocity spectrum (without any spatial average) is also represented (black line).

velocity field exhibits a power-law decay of $-7/3$ in the inertial range when a sufficient number of points per integral length scale is considered (at least $N_p L_u/L_p \geq 90$), regardless of the number of statistically independent velocity samples (even in the case of $L_p < L_u$). It is also shown that when the domain

length is smaller than the integral length scale, the power law decay exponent $-7/3$ is preferentially observed.
Even if such a result might be generalized in the presence of a non-homogeneous direction, further studies are required to confirm it. Indeed, it is assumed that the nature of the shear may certainly play a non-negligible effect on the spatial averaging procedure. Furthermore, the number of points per integral length scale and its consequence on the resulting spatially averaged velocity spectrum would certainly also depend on the nature of the shear and its associated (possibly varying) integral length scale(s) along this non-homogeneous direction.

5. Conclusion

A synthetic velocity database designed to reproduce a realistic ABL turbulent flow was designed with the aim of investigating the effect of spatial integration on the velocity spectrum. The interest of such a synthetic database was inferring previous experimental results, as it allowed some crucial physical parameters to be properly adjusted. The generated 2D velocity database was supposed to have an integral length scale larger than the length of the computational domain that is greater than a rotor diameter. In this case, it was demonstrated for a non-homogeneous turbulent flow satisfying Kolmogorov's "$-5/3$ law", that the velocity spectrum of the spatially averaged velocity field along N direction(s) had an inertial slope of $-5/3 - 2N/3$. Furthermore, this synthetic database was used to assess an equivalent turbine thrust spectrum by considering a 2D spatial averaging (over blade area) coupled with an average over the number of blades of the synthetic velocity field. It was confirmed that such an equivalent turbine thrust spectrum exhibited a power-law decay exponent of $-11/3$ in the inertial range. As the turbine thrust and turbine power theoretically have a similar dependence on the instantaneous velocity field (Druault et al., 2022), the turbine power spectrum also exhibits a power-law decay of $-11/3$ in the inertial frequency range.
As the spatial averaging procedure and its consequences on the resulting spectrum depend on the velocity sample statistical independence and/or the number of points per integral flow length scale, 1D databases were also generated to study this effect. We then demonstrated that the additional $-2/3$ in the spatially averaged velocity spectrum was favorably observed when a sufficient number of points (greater than 90) was used to describe the integral length scale, even when the length of the domain was smaller than the integral length scale of the flow. It was also shown that the spatial averaging effect was not dependent on the number of statistically independent velocity samples. In contrast, in the presence of an infinite number of independent samples, spatial averaging of velocity samples would lead to recovery of the initial power-law decay of the one-point velocity sample, that is, $-5/3$. Some similar studies have now to be done to analyze similar effects along a non-homogeneous direction.
Finally, these last results tend to confirm that the power law decay of $-11/3$ observed in the inertial range of the turbine power spectrum can be a consequence of the spatial averaging procedure under the condition that a sufficient

number of measurement or numerical grid points are used to properly describe the rotor blade and linked to the value of the integral flow length scale.
As a future work, a mathematical theory should be developed to explain the $-2N/3$ subtraction observed in the spatially averaged velocity spectrum when the average operation is done over N anisotropic non-homogeneous directions.

References

Adcok, T., Draper, S., Willden, R., Vogel, C., 2020. The fluid mechanics of tidal stream energy conversion. Annu. Rev. Fluid Mech 53, 287–310.

Bandi, M. M., 2017. Spectrum of Wind Power Fluctuations. Physical Review Letters 118 (2), 1–5.

Bossuyt, J., Meneveau, C., Meyers, J., 2017. Wind farm power fluctuations and spatial sampling of turbulent boundary layers. Journal of Fluid Mechanics 823, 329–344.

Chamorro, L. P., Hill, C., Neary, V. S., Gunawan, B., Arndt, R. E., Sotiropoulos, F., 2015. Effects of energetic coherent motions on the power and wake of an axial-flow turbine. Physics of Fluids 27 (5), 1–12.

Cheynet, E., 2018. Wind field simulation (the fast version). https://se.mathworks.com/matlabcentral/fileexchange/68632-wind-field-simulation-the-fast-version.

Davenport, A., 1961. The spectrum of horizontal gustiness near the ground in high wind. Quart. J.R. Met. Soc. 87, 194–211.

Druault, P., Gaurier, B., Germain, G., 2022. Spatial integration effect on velocity spectrum: Towards an interpretation of the $-11/3$ power law observed in the spectra of turbine outputs. Renewable Energy 181, 1062–1080.

Druault, P., Germain, G., 2022. Experimental investigation of the upstream turbulent flow modifications in front of a scaled tidal turbine. Renewable Energy Renewable Energy 196, 1204–1217.

Druault, P., Germain, G., 2022. Prediction of the tidal turbine power fluctuations from the knowledge of incoming flow structures. Ocean Eng. 252, 111180.

Gaurier, B., Ikhennicheu, M., Germain, G., Druault, P., 2020. Experimental study of bathymetry generated turbulence on tidal turbine behaviour. Renewable Energy 156, 1158–1170.

Hekmati, A., Ricot, D., Druault, P., 2013. Numerical synthesis of aeroacoustic wall pressure fields over a flat plate: Generation, transmission and radiation analyses. J. Sound and Vibration. 332 (13), 3163–3176.

Kaimal, J., Finnigan, J., 1994. Atmospheric boundary layer flows: Their structure and measurement. Oxford University Press.

Kaimal, J., Wyngaard, J., Izumi, Y., Coté, O., 1972. Spectral characteristics of surface-layer turbulence. Quart. J.R. Met. Soc. 98, 563–589.

Katzenstein, W., Fertig, E., Apt, J., 2010. The variability of interconnected wind plants. Energy Policy 38 (8), 4400–4410.

Liu, H., Jin, Y., Tobin, N., Chamorro, L. P., 2017. Towards uncovering the structure of power fluctuations of wind farms. Physical Review E 96 (6), 3–8.

Mann, J., 1994. The Spatial Structure of Neutral Atmospheric Surface-Layer Turbulence. Journal of Fluid Mechanics 273, 141–168.

Mann, J., 1998. Wind field simulation. Prob. Engng. Mech. 13 (4), 269–282.

Myrtvedt, M., Nybo, A., Nielsen, F., 2020. The dynamic response of offshore wind turbines and their sensitivity to wind field models. J. Phys.: Conf. Ser. 1669, 012013.

Paraz, F., Bandi, M. M., 2019. Second order structure functions for higher powers of turbulent velocity. Journal of Physics Condensed Matter 31 (48).

Simiu, E., Potra, F.A., Nandi, T.N. 2019. Determining Longitudinal Integral Turbulence Scales in the Near-Neutral Atmospheric Surface Layer Bound. Layer Meteo. 170 (2), 349-355.

Sorensen, N., Schreck, S., 2014. Transitional ddes computations of the nrel phase-vi rotor in axial flow conditions. J. Phys.: Conf. Ser. 555, 012096.

Sorensen, P., Hansen, A., Carvalho Rosas, P., 2002. Wind models for simulation of power fluctuations from wind farms. J. Wind Eng. Ind. Aerodynamics 90, 1381–1402.

Thé, J., Yu, H., 2017. A critical review on the simulations of wind turbine aerodynamics focusing on hybrid rans-les methods. Energy 138, 257–289.

Tobin, N., Zhu, H., Chamorro, L. P., 2015. Spectral behaviour of the turbulence-driven power fluctuations of wind turbines. Journal of Turbulence 16 (9), 832–846.